Constitutive parameter retrieval for uniaxial metamaterials with spatial dispersion

Achiles F. Mota,[1] Augusto Martins,[1] John Weiner,[2] Fernando L. Teixeira,[3] and Ben-Hur V. Borges[1,*]

[1]*Department of Electrical and Computer Engineering, University of São Paulo, SP, CEP 13566-590, Brazil*

[2]*Physics Institute of São Carlos, University of São Paulo, SP, CEP 13566-590, Brazil*

[3]*ElectroScience Laboratory, The Ohio State University, Columbus, Ohio 43210, USA*

(Received 5 May 2016; revised manuscript received 20 July 2016; published 6 September 2016)

We propose a constitutive parameter retrieval approach in which all electromagnetic parameters of the medium are obtained taking spatial dispersion into account. Moreover, the constraint on nonmagnetic metal/dielectric metamaterials is relaxed. This procedure is applied to metal/dielectric stacks in order to address the effects of the layer thickness, layer number, and material choice on the spatial dispersion. The results demonstrate that the investigated metal/dielectric stacks have a clear magnetic response, particularly for thicker layers. Moreover, this magnetic response is also a function of the magnitude of the $|k_x/k_0|$ ratio, where k_x is the wave vector parallel to the interface planes and k_0 is the free-space wave number. We demonstrate that the real part of the dispersion curve flattens out (with a corresponding large imaginary part being present) as a result of the absence of propagating modes inside the metamaterial. This flat region is strongly dependent on the thickness of the layers and is a direct manifestation of spatial dispersion. Using this parameter retrieval method we calculate the Purcell factor for Rb atoms 10 nm above the surface of a Ag/TiO_2 stack with two filling factors ρ [$\rho = l/(l+d)$ with l and d as the metal and dielectric layer thicknesses, respectively], $\rho = 0.3$ and $\rho = 0.5$, and having $N = 13$ layers, for the emission wavelengths of 435 nm and 785 nm. Results are then compared with three different approaches, and we show that if spatial dispersion is not properly taken into account, then the Purcell factor is overestimated. Our approach shows excellent agreement with Purcell factors obtained from precise and accurate numerical calculations of the corresponding nonhomogenized structures.

DOI: 10.1103/PhysRevB.94.115410

I. INTRODUCTION

Recently, a special class of metamaterials, formally known as hyperbolic metamaterials (HMM), has attracted a great deal of attention, particularly at optical frequencies [1]. In addition to producing negative refraction [2,3], HMMs can be used as hyperlenses [4,5] and, more importantly, to increase the photonic density of states [6–9]. This last application will be explored later on in this paper. HMMs are also extremely anisotropic, having opposite signs for the parallel and perpendicular components of their permittivity tensor [3]. The term hyperbolic metamaterial is derived from the hyperbolic (as opposed to ellipsoidal or spherical) dispersion profile of the isofrequency surface. Two different approaches are normally used to experimentally realize this profile. The first is through a wired medium and the second is through a planar stack of metal/dielectric layers [1,3]. The shape of the hyperboloid (either single or double sheeted) can be easily controlled by an appropriate choice of wavelength, materials, and geometry. However, the extraction of effective parameters (homogenization) of such metamaterial media has proved to be a challenging task [10–15].

The simplest homogenization approach, particularly for HMMs, is to utilize effective medium theory (EMT) [16]. Unfortunately, good homogeneity can only be obtained if the thickness of the layers is much smaller than the operating wavelength [17]. In contrast, a comprehensive parameter retrieval approach has recently been proposed by Papadakis *et al.* [15]. These authors propose a general approach for retrieving the effective permittivity tensor of uniaxial anisotropic metamaterials without the need for assuming nonmagnetic metal/dielectric metamaterials. However, this approach assumes the stack exhibits no spatial dispersion (with spatial dispersion being defined as the phenomenon whereby the permittivity and/or permeability tensors of the medium depend on the wave vector k [18]). Chebykin *et al.* [12] have shown that when $k > k_0$, spatial dispersion becomes an issue that can no longer be neglected. The importance of taking spatial dispersion into account can be fully understood if, for instance, the enhancement of the Purcell factor is of interest [6–9]. The accurate calculation of the Purcell factor requires the reflection coefficient to be computed even for values of k much greater than k_0.

In this paper, we propose a parameter retrieval approach in which all electromagnetic parameters of the medium are obtained taking spatial dispersion into account. This approach is from hereon named a complete parameter retrieval approach, or CPR. As in [15], the constraint on nonmagnetic metal/dielectric metamaterials is also relaxed. We investigate different metal/dielectric stacks and show that all of them have a clear magnetic response, particularly for thicker layers. We also show that a large $|k_x/k_0|$ causes the dispersion curve to flatten out (with a corresponding large imaginary part being present) as a result of the absence of propagating modes inside the metamaterial. This behavior is a direct manifestation of spatial dispersion. We also investigate how spatial dispersion impacts the calculation of the Purcell factor of Rb atoms 10 nm above the HMM surface for the emission wavelengths of 435 nm and 785 nm. The results are compared with three different approaches, namely, the accurate result considering the actual nonhomogenized geometry, the approach in [15], and the EMT approach. We show that if spatial dispersion is not properly taken into account the Purcell factor is overestimated.

*benhur@sc.usp.br

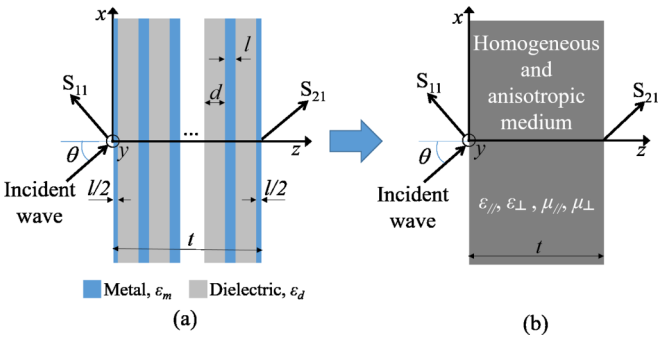

FIG. 1. (a) Metal/dielectric stack with incident wave impinging on the surface from the left. Part of the incident wave is reflected (S_{11}) and part is transmitted (S_{21}). The metal and dielectric thicknesses are l and d, respectively. (b) Equivalent homogenous anisotropic medium.

In contrast, the CPR approach shows excellent agreement with the accurate Purcell factor.

This paper is organized as follows. In Sec. II we lay out the mathematical formalism of the proposed parameter retrieval approach. In Sec. III we analyze different metal/dielectric stacks as a function of the metal thickness and fill factor. We also discuss the role of the number of layers on the performance of the parameter retrieval approach. Section IV deals with the calculation of the Purcell factor, showing a comparison between the results obtained both with the EMT and with the CPR approach. Finally, Sec. V presents some concluding remarks.

II. EXTRACTION PROCEDURE

The CPR approach assumes that the metal/dielectric stack of Fig. 1(a) can be equivalently represented by the homogeneous, uniaxial anisotropic medium shown in Fig. 1(b), with both media expected to produce the same scattering parameters (S-parameters). The present approach works as follows: we first calculate the S-parameters for both structures in Fig. 1 (see Secs. II A and II B below), and then we combine the corresponding equations (Sec. II C) so that expressions for the permittivity and permeability tensor components of the homogenous medium can be obtained. The procedure is carried out for both TE and TM polarizations simultaneously, since the extracted parameters are assumed to be the same for both polarizations. This allows us to relax the constraint on nonmagnetic metal/dielectric metamaterials.

A. S-parameters of the metal-dielectric stack

The extraction procedure begins with the calculation of the S-parameters for both polarizations, TE (S_{11}^{TE}, S_{21}^{TE}) and TM (S_{11}^{TM},S_{21}^{TM}), of the metal-dielectric stack with dielectric thickness d and metal thickness l [Fig. 1(a)]. The CPR approach assumes the stack as symmetric so that $S_{11} = S_{22}$ and $S_{21} = S_{12}$. As a result, and in order to keep the fill factor $\rho = l/(l+d)$ unchanged, the thickness of the first and last layers of the stack must be half the metal thickness ($l/2$). Considering a stack of N layers, with metal and dielectric relative permittivities ϵ_m and ϵ_d, respectively, the S-parameters are obtained as follows [1]:

$$\begin{bmatrix} 1 \\ S_{11}^{\Delta} \end{bmatrix} = \left(D_0^{\Delta}\right)^{-1} T^{\Delta} D_{N+1}^{\Delta} \begin{bmatrix} S_{21}^{\Delta} \\ 0 \end{bmatrix}, \tag{1}$$

where the index Δ stands for TE or TM polarization, and

$$T^{\Delta} = \prod_{p=1}^{N} D_p^{\Delta} P_p \left(D_p^{\Delta}\right)^{-1}, \tag{2}$$

$$D_p^{TM} = \begin{bmatrix} 1 & 1 \\ \frac{k_z^p}{\epsilon_p} & -\frac{k_z^p}{\epsilon_p} \end{bmatrix}, \tag{3}$$

$$D_p^{TE} = \begin{bmatrix} 1 & 1 \\ k_z^p & -k_z^p \end{bmatrix}, \tag{4}$$

$$P_p = \begin{bmatrix} e^{-jk_z^p d_p} & 0 \\ 0 & e^{jk_z^p d_p} \end{bmatrix}, \tag{5}$$

with $\epsilon_p = \epsilon_m$ (for p odd) or $\epsilon_p = \epsilon_d$ (for p even), k_z^p is the wave vector in the z direction inside the pth layer, and d_p is the thickness of the pth layer (with $d_1 = d_N = l/2$). The parameter extraction is performed as a function of the wave vector in the x direction (k_x) in order to visualize the effects of the spatial dispersion in the HMM. This choice is justified since the boundary conditions for k_x require this wave vector to be the same (phase matching) in all layers of the stack [Fig. 1(a)] and inside the anisotropic metamaterial [Fig. 1(b)]. As such, k_z^p can be calculated from the following relation:

$$k_z^p = \sqrt{k_0^2 \epsilon_p - k_x^2}. \tag{6}$$

B. S-parameters of the anisotropic medium

The next step consists in calculating the S-parameters of the metal/dielectric stack, treated here as a homogeneous and anisotropic slab with thickness t [Fig. 1(b)]. The relative permittivity and permeability tensors of an anisotropic media can be written as $\bar{\bar{\epsilon}} = \mathrm{diag}[\epsilon_x,\epsilon_y,\epsilon_z]$ and $\bar{\bar{\mu}} = \mathrm{diag}[\mu_x,\mu_y,\mu_z]$, respectively. Due to the symmetry of the stack [Fig. 1(a)], it follows that $\epsilon_x = \epsilon_y = \epsilon_\perp$, $\epsilon_z = \epsilon_{||}$, $\mu_x = \mu_y = \mu_\perp$, and $\mu_z = \mu_{||}$. Since the anisotropic medium is uniaxial, the TE (E_y, H_x, H_z) and TM (H_y, E_x, E_z) solutions can be decoupled. Therefore, we start with the wave equations TE and TM polarization, which are written, respectively, as

$$\frac{1}{\mu_\perp}\frac{\partial^2 E_y}{\partial z^2} + \frac{1}{\mu_{||}}\frac{\partial^2 E_y}{\partial x^2} + E_y k_0^2 \epsilon_\perp = 0, \tag{7}$$

$$\frac{1}{\epsilon_\perp}\frac{\partial^2 H_y}{\partial z^2} + \frac{1}{\epsilon_{||}}\frac{\partial^2 H_y}{\partial x^2} + H_y k_0^2 \mu_\perp = 0. \tag{8}$$

The $(\vec{k},\omega)$ dependence relative to E_y, H_y, $\epsilon_{\perp,||}$, and $\mu_{\perp,||}$ is omitted for the sake of simplicity. The solutions of (7) and (8) for TE and TM polarizations are, respectively,

$$E_y = E_0 e^{j(\beta_z^{TE} z + \beta_x^{TE} x)}, \tag{9}$$

$$H_y = H_0 e^{j(\beta_z^{TM} z + \beta_x^{TM} x)}, \tag{10}$$

where E_0 and H_0 are the amplitudes of the electric (TE) and magnetic (TM) fields; β_z^{TE}, β_x^{TE}, β_z^{TM}, and β_x^{TM} are the z and

x components of the wave vector. After substituting (9) into (7) and (10) into (8), the dispersion relations for TE and TM modes, respectively, become

$$\frac{\left(\beta_z^{TE}\right)^2}{\mu_\perp} + \frac{\left(\beta_x^{TE}\right)^2}{\mu_\parallel} = k_0^2 \epsilon_\perp, \tag{11}$$

$$\frac{\left(\beta_z^{TM}\right)^2}{\epsilon_\perp} + \frac{\left(\beta_x^{TM}\right)^2}{\epsilon_\parallel} = k_0^2 \mu_\perp. \tag{12}$$

We should note that spatially dispersive media often necessitate additional boundary conditions (ABCs) according to the specific type of spatial dispersion model assumed [19–24]. In particular, ABCs are invoked in the most common spatial dispersion model, viz. the isotropic[1] nonlocal hydrodynamic Drude model [25] and its variants, since this model supports longitudinal modes, which calls for enforcing either the normal component of current density to be zero at the material interface (in models supporting eddy currents [25]), or for enforcing both the normal and tangential current components to be zero at the material interface (in models not supporting eddy currents [26]).

Here, spatial dispersion is treated not from a first-principles hydrodynamic model but instead as a direct consequence of an S-parameter extraction, homogenization, and inversion procedure. In particular, we do not invoke an isotropic spatially dispersive model but extract optical parameters from a homogenized, highly anisotropic (uniaxial) material by an inversion procedure of S-parameters determined by the application of conventional boundary phase-matching conditions to a periodic stack of alternating metal and dielectric slabs. Optical excitation in a frequency regime far below collective polariton resonances, where the extra transverse and longitudinal wave amplitudes are negligible [19,20], permit the application of conventional phase-matching conditions at surfaces to determine the effective medium parameters.[2] A similar procedure has been applied previously [27]. Next, we calculate the reflection and transmission coefficients for both TM and TE polarizations as depicted in Figs. 2(a) and 2(b), respectively. In both polarizations, the incident wave travels in air from the left with wave vector components k_x and k_z [given by (6) with $\epsilon_p = 1$]. The wave gets partially reflected (superscript r) and partially transmitted (superscript t) into the anisotropic medium. As a result, after imposing the continuity

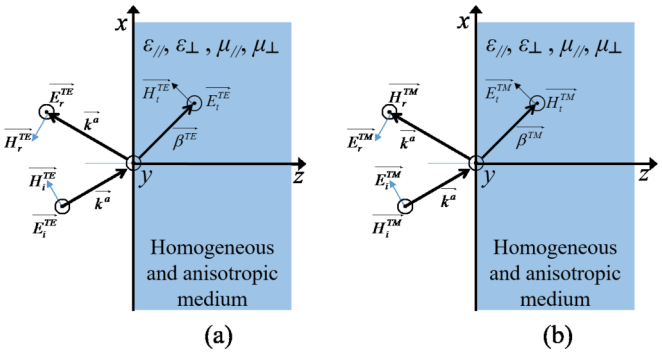

FIG. 2. Diagrams show field components incident on the interface between air and a homogenous, anisotropic medium for (a) TE and (b) TM polarizations.

of tangential components on the interface, the following set of equations is obtained for both TE and TM polarizations:

$$\begin{aligned}
A_y^i &= A_0 e^{j(k_x x + k_z z)},\\
A_y^r &= R_\Delta A_0 e^{j(k_x x - k_z z)},\\
A_y^t &= T_\Delta A_0 e^{j(\beta_x^\Delta x + \beta_z^\Delta z)},\\
B_x^i &= -A_0 \frac{k_z}{\omega \delta_0} e^{j(k_x x + k_z z)},\\
B_x^r &= R_\Delta A_0 \frac{k_z}{\omega \delta_0} e^{j(k_x x - k_z z)},\\
B_x^t &= -T_\Delta A_0 \frac{\beta_z^\Delta}{\omega \delta_0 \delta_\perp} e^{j(\beta_x^\Delta x + \beta_z^\Delta z)},
\end{aligned} \tag{13}$$

where R_Δ and T_Δ are the reflection and transmission coefficients, respectively, A is assumed as E (for TE) or H (for TM), B is assumed as H (for TE) or $-E$ (for TM), and δ is assumed as μ (for TE) or ϵ (for TM). The boundary relationships impose the following relation:

$$k_x = \beta_x^{TM} = \beta_x^{TE}. \tag{14}$$

With the help of the boundary relationships for the tangential field components, the following equations for R_Δ and T_Δ are obtained:

$$R_\Delta = \frac{Z_\Delta - 1}{Z_\Delta + 1}, \tag{15}$$

$$T_\Delta = 1 - R_\Delta, \tag{16}$$

$$Z_\Delta = \frac{k_z \alpha}{\beta_z^\Delta}, \tag{17}$$

where α assumes $\mu_\perp$ for TE or $\epsilon_\perp$ for TM polarization. Once the transmission and reflection coefficients are calculated, the scattering parameters for the slab of a homogeneous and anisotropic media with thickness t can be obtained as follows [28]:

$$S_{11}^\Delta = \frac{R_\Delta (1 - e^{2j\beta_z^\Delta t})}{1 - R_\Delta^2 e^{2j\beta_z^\Delta t}}, \tag{18}$$

$$S_{21}^\Delta = \frac{\left(1 - R_\Delta^2\right) e^{j\beta_z^\Delta t}}{1 - R_\Delta^2 e^{2j\beta_z^\Delta t}}. \tag{19}$$

[1]Despite being typically represented in tensorial form, the hydrodynamic Drude model is isotropic since the two terms of the tensor expression represent longitudinal and transverse permittivity expression with respect to the propagation vector and not to any preferential direction of space.

[2]On the subject of ABCs, we should note in passing that ABCs are also necessitated in some types on anisotropic spatially dispersive media obtained from homogenization procedures such as wire media [23]. However, in such media the required ABC is again for the normal component of current density to be zero at the material interface because of the existence of longitudinal current modes along the metal wires. In our problem, the metal layers are transverse, and as such, longitudinal currents modes are not supported, obviating the need for such condition.

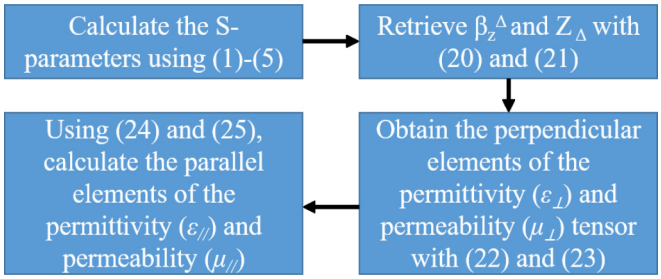

FIG. 3. Diagram shows the algorithm for extracting constitutive parameters.

C. Extraction of the constitutive parameters from the S-parameters of the slab

At this point, both the S-parameters of the stack [Fig. 1(a)] and of its homogenized slab [Fig. 1(b)] have been obtained. In order to extract the constitutive parameters, Eqs. (18) and (19) must be solved for β_z^{Δ} and Z_{Δ} as functions of S_{11}^{Δ} and S_{21}^{Δ}. Thus, after inverting (18) and (19) we get [10]

$$Z_{\Delta} = \pm\sqrt{\frac{\left(1+S_{11}^{\Delta}\right)^2-\left(S_{21}^{\Delta}\right)^2}{\left(1-S_{11}^{\Delta}\right)^2-\left(S_{21}^{\Delta}\right)^2}}, \tag{20}$$

$$\beta_z^{\Delta} = \frac{1}{t}\left\{\cos^{-1}\left(\frac{1}{2S_{21}^{\Delta}}\left[1-\left(S_{11}^{\Delta}\right)^2+\left(S_{21}^{\Delta}\right)^2\right]\right)+2\pi n\right\}, \tag{21}$$

where the sign of (20) is chosen so as to satisfy $\mathrm{Re}\{Z_{\Delta}\} > 0$, and n is an integer obtained via the phase-unwrapping method [11]. Thus $\mu_{\perp}$ and $\epsilon_{\perp}$ are obtained from (17) as follows:

$$\mu_{\perp} = \frac{Z_{TE}\beta_z^{TE}}{k_z}, \tag{22}$$

$$\epsilon_{\perp} = \frac{Z_{TM}\beta_z^{TM}}{k_z}. \tag{23}$$

Finally, using (11) and (12), the remaining parameters ($\mu_{||}$ and $\epsilon_{||}$) are obtained as follows:

$$\mu_{\parallel} = \frac{k_x^2\mu_{\perp}}{k_0^2\mu_{\perp}\epsilon_{\perp}-\left(\beta_z^{TE}\right)^2}, \tag{24}$$

$$\epsilon_{\parallel} = \frac{k_x^2\epsilon_{\perp}}{k_0^2\mu_{\perp}\epsilon_{\perp}-\left(\beta_z^{TM}\right)^2}. \tag{25}$$

The algorithm for the extraction of the constitutive parameters of a metamaterial is diagramed in Fig. 3.

III. RESULTS

The most outstanding feature of hyperbolic metamaterials is the existence of photonic states with wave vector (k) much greater than the free-space wave vector (k_0). These high-k modes can be excited, for instance, by placing a dipole close to the HMM surface [29]. Since the dipole radiation is a superposition of propagating ($k_x \leqslant k_0$) and evanescent ($k_x \geqslant k_0$) waves, if the dipole is sufficiently close to the surface its evanescent waves will couple to the high-k states of the HMM. This characteristic is extremely important for the enhancement of the Purcell factor [6–9]. Consequently, it becomes crucial to understand the electromagnetic behavior of the HMM for all possible ranges of k_x.

According to [15], whenever the parameter extraction is carried out in the region of low k_x ($k_x \leqslant k_0$), the spatial dispersion does not really constitute a problem. However, $k_x \geqslant k_0$ implies lower effective wavelengths inside the HMM, thus making spatial dispersion a subject requiring further investigation. The CPR approach takes this problem into consideration and explores three different cases to highlight its influence on the extracted parameters, namely, the effect of the layers' thickness, the effect of the number of layers, and, finally, the effect of the metal/dielectric composition. This will allow us to clearly show how the spatial dispersion behavior for high values of k_x is manifested.

A. Influence of the dielectric thickness

In this section, we investigate the effect of the dielectric thickness on the extracted parameters obtained with three different approaches, namely, the EMT (solid line, stars), the approach in [15] (dashed lines, hollow symbols), and the CPR approach (solid lines, full symbols). The EMT has been widely used in the literature to calculate the electromagnetic parameters of metal/dielectric stacks [16] and assumes that the dielectric and metal thicknesses are much smaller than the wavelength. In [15], the authors restricted their results to the region $k_x \leqslant k_0$. For the sake of comparison, we have extrapolated their approach for cases with $k_x \geqslant k_0$.

In the examples discussed in this section, two different filling factors are considered, i.e., $\rho = 0.1$ and $\rho = 0.3$. The wavelength is 780 nm, the dielectric is TiO_2 ($\epsilon_d = 6.375\,2$), the metal is Ag ($\epsilon_m = -29.36 + 0.35\,j$), and the number of layers is 21. Figure 4 shows the extracted parameters of the Ag/TiO_2 stack for $\rho = 0.1$. The real and imaginary parts of $\epsilon_{\perp}$, $\epsilon_{||}$, $\mu_{\perp}$, and $\mu_{||}$ are shown in Figs. 4(a)–4(h) for $d = 15$ nm (squares), $d = 30$ nm (circles), and $d = 45$ nm (triangles). For the results obtained with the EMT approximation it is assumed $\mu = 1$. Note that since ρ is constant, the permittivity obtained with the EMT is invariant to k. In addition, Figs. 4(e) and 4(g) show that the assumption of $\mu = 1$ is actually valid only for small values of d. The soundness of the CPR approach can be further verified by noting that $\epsilon_{\perp}$ and $\epsilon_{||}$ tend to those of the EMT when the dielectric thickness is very small (which is actually the condition for the EMT approximation to be valid). In [15] the authors consider $\epsilon_{\perp}$ and $\mu_{\perp}$ as constants for any value of k_x, justified by the absence of spatial dispersion [Figs. 4(a,b) and 4(e,f), dashed lines, hollow symbols). Considering the interval $|k_x/k_0| < 1$, we notice that $\epsilon_{||}$ and $\mu_{||}$ present little variation, meaning that spatial dispersion is small in this region [Figs. 4(c,d) and 4(g,h), dashed lines, hollow symbols]. However, even in the interval $|k_x/k_0| < 1$ the parameters extracted with [15] do not agree with those predicted with the CPR approach, especially for thicker dielectric layers. Yet, if $\epsilon_{\perp}$ and $\mu_{\perp}$ are assumed constant, $\epsilon_{||}$ and $\mu_{||}$ will be incorrectly calculated because even small perturbations in $\epsilon_{\perp}$ and $\mu_{\perp}$ can cause large variations in (24) and (25). By analyzing the results of the CPR approach it becomes clear that all

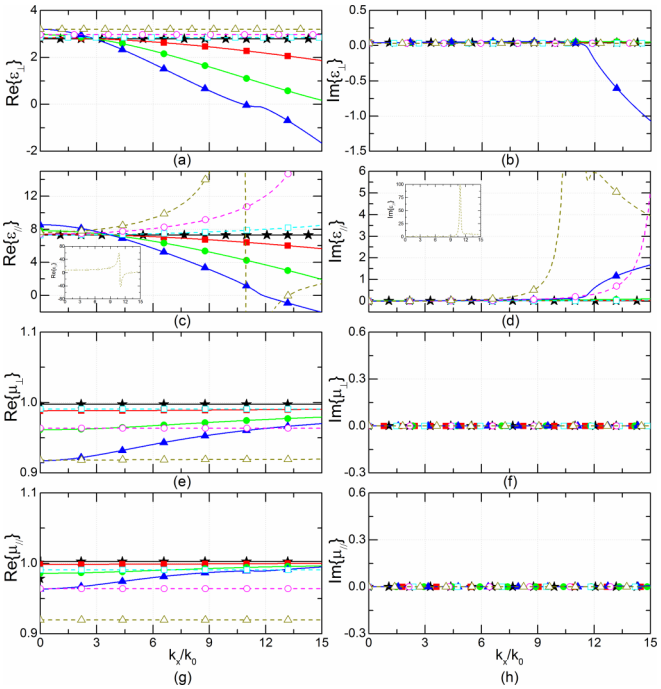

FIG. 4. Real (left column) and imaginary (right column) parts of the extracted electromagnetic parameters of a layered medium of Ag/TiO_2 with $\rho = 0.1$ for dielectric thickness of 15 (squares), 30 (circles), and 45 nm (triangles) for [15] (dashed lines, hollow symbols) and the CPR approach (solid lines, full symbols). (a,b) $\epsilon_\perp$, (c,d) $\epsilon_{||}$, (e,f) $\mu_\perp$, and (g,h) $\mu_{||}$. The EMT (solid line, stars) results are also plotted for comparison. The inset in (c,d) shows the full magnitude of the real and imaginary parts of $\epsilon_{||}$ for the 45-nm case of [15].

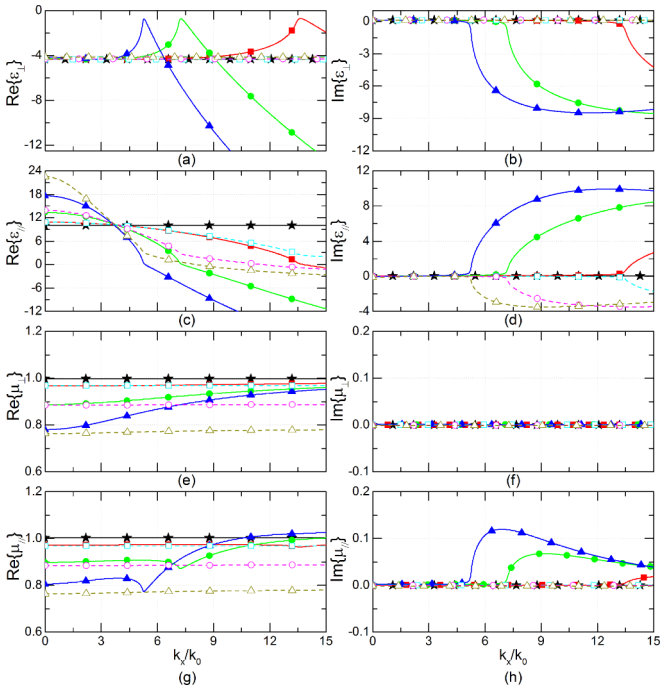

FIG. 5. Real (left column) and imaginary (right column) parts of the extracted electromagnetic parameters of a layered medium of Ag/TiO_2 with $\rho = 0.3$ for dielectric thickness of 15 (squares), 30 (circles), and 45 nm (triangles) for [15] (dashed lines, hollow symbols) and the CPR approach (solid lines, full symbols. (a,b) $\epsilon_\perp$, (c,d) $\epsilon_{||}$, (e,f) $\mu_\perp$, and (g,h) $\mu_{||}$. The EMT (solid line, stars) results are also plotted for comparison.

electromagnetic parameters vary with k_x, which characterizes spatial dispersion. In addition, spatial dispersion is so critical that it can even cause $\epsilon_\perp$ and $\epsilon_{||}$ to change sign ($|k_x/k_0| = 11.9$ for $\epsilon_{||}$ and $|k_x/k_0| = 10.8$ for $\epsilon_\perp$; see the plotted triangles curve in Fig. 4 for $d = 45$ nm). When a sign change occurs, the losses increase very rapidly and the incident wave interacts almost entirely with the initial layers of the stack. For this reason, the higher the $|k_x/k_0|$ ratio, the more the extracted parameters will tend toward those of the first layer (metal in this case). Furthermore, notice that the magnitude of the imaginary part of $\epsilon_\perp$ decreases rapidly for $|k_x/k_0| > 10.8$, while that of $\epsilon_{||}$ grows very quickly in the region $|k_x/k_0| > 11.9$ for $d = 45$ nm (triangles curve in Fig. 4). The increase in the metal thickness enhances the magnetic behavior of this material, causing a decrease in the permeability values as seen in Figs. 4(e) and 4(g). Next, we extract the electromagnetic parameters of the TiO_2/Ag stack with $\rho = 0.3$. The real and imaginary parts of $\epsilon_\perp$, $\epsilon_{||}$, $\mu_\perp$, and $\mu_{||}$ are shown in Figs. 5(a)–5(h) for $d = 15$ nm (squares), $d = 30$ nm (circles), and $d = 45$ nm (triangles). Once more, the values of $\epsilon_\perp$ and $\epsilon_{||}$ tend to those of the EMT (and $\mu_\perp$ and $\mu_{||}$ tend to 1) only when the dielectric thickness tends to zero. By observing Figs. 5(e) and 5(g) it becomes clear that the assumption of $\mu = 1$ is not valid because the stack does show magnetic response, particularly for thicker layers. Moreover, these results show that the extracted parameters can be incorrectly calculated even for $|k_x/k_0| < 1$ [Figs. 5(c) and 5(g)] if spatial dispersion is not taken into account. Despite the differences mentioned above, all three approaches predict a hyperbolic dispersion profile for this structure ($\epsilon_\perp < 0$ and $\epsilon_{||} > 0$) for low values of $|k_x/k_0|$. Nevertheless, for $d = 30$ nm, the CPR approach predicts a change in the shape of the dispersion curve for $|k_x/k_0| > 7.5$ because $\epsilon_{||}$ becomes smaller than zero [Fig. 5(c)]. The same phenomenon occurs for $d = 45$ nm and $|k_x/k_0| > 5.3$, and for $d = 15$ nm and $|k_x/k_0| > 14$. As explained, the electromagnetic parameters tend to those of the first layer (a metal in this case, with $\epsilon_\perp < 0$ and $\epsilon_{||} < 0$) for increasing $|k_x/k_0|$ values.

The peaks and inflection points in Figs. 5(a) and 5(c), respectively, as well as the valleys in Fig. 5(g), only appear if spatial dispersion is properly taken into account in the parameter retrieval procedure. This effect will be further explored in Sec. IV with the calculation of the Purcell factor.

B. Influence of the number of layers

In this section, the effect of the number of layers on the design and performance of hyperbolic metamaterials is investigated. Again, the results are obtained with the EMT (solid line, stars), [15] (dashed lines, hollow symbols), and the CPR approach (solid lines, full symbols). The structure consists of a stack of Ag/TiO_2 with $d = 20$ nm, $\rho = 0.3$, and wavelength $\lambda = 780$ nm. Different numbers of layers are considered, i.e., 3 (squares), 15 (circles), and 27 (triangles). The results for the real and imaginary parts of ($\epsilon_{||}$, $\epsilon_\perp < 0$) are

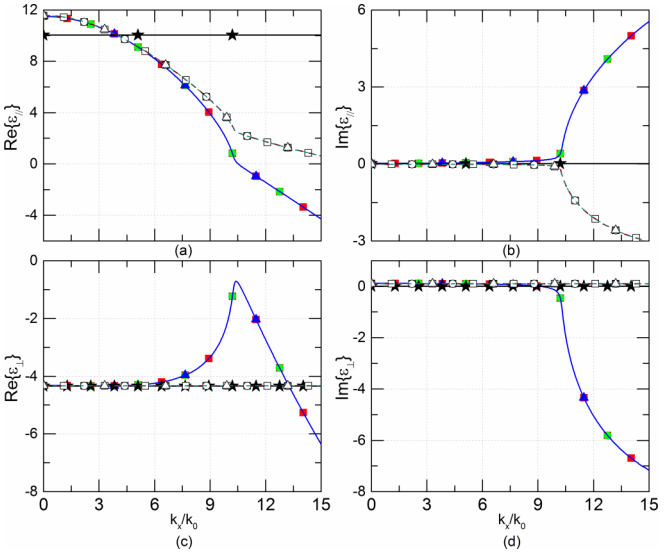

FIG. 6. Real (left column) and imaginary (right column) parts of (a) $\epsilon_{||}$ and (b) $\epsilon_{\perp} < 0$ for 3 (squares), 15 (circles), and 27 (triangles) layers for [15] (dashed lines, hollow symbols) and the CPR approach (solid lines, full symbols). The EMT (solid line, stars) results are also plotted for comparison.

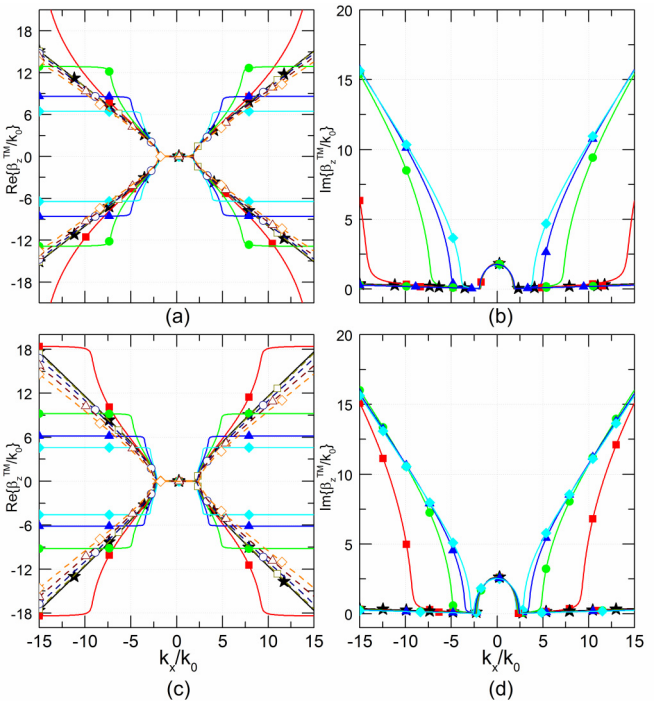

FIG. 7. Real (left column) and imaginary (right column) parts of the dispersion curves of a Ag/SiO_2 stack with $\rho = 0.3$ (a,b) and $\rho = 0.5$ (c,d). The dielectric thicknesses (used as a parameter) is 8 nm (squares), 16 nm (circles), 24 nm (triangles), and 32 nm (diamonds) for [15] (dashed lines, hollow symbols) and the CPR approach (solid lines, full symbols). Results from the EMT (solid line, stars) are also shown for comparison.

shown in Figs. 6(a,c) and 6(b,d), respectively. Regardless of the approach, the change in the number of layers does not modify the effective parameters, thus keeping R_Δ and Z_Δ unaltered according to (15) and (17). However, the scattering parameters do change because the total thickness of the slab increases with the increase in the number of layers according to (18) and (19). Additionally, Figs. 6(a) and 6(b) show how the spatial dispersion impacts the magnitude of the retrieved parameters, an effect that is not observed with the EMT approximation or with the approach of [15] for $\epsilon_{||}$. When d is small, [15] shows good accuracy only in the region $|k_x/k_0| < 1$.

C. Analysis of the dispersion curves

As discussed earlier, hyperbolic metamaterials can support solutions with $k_x \gg k_0$. However, because of spatial dispersion, there are regions of high k_x where the layered medium is highly lossy and wave propagation is not supported. In order to better understand this condition, we investigate a stack of Ag/SiO_2 ($\epsilon_d = 2.126$ and $\epsilon_m = -16.075 + 0.437j$) with $\rho = 0.3$ and $\rho = 0.5$ at $\lambda = 600$ nm for different dielectric thicknesses (8, 16, 24, and 32 nm) and TM polarization. The real (left column) and imaginary (right column) parts of the dispersion curves obtained with the CPR approach (solid lines, full symbols) are shown in Fig. 7. Results with the EMT (solid line, stars) and [15] (dashed lines, hollow symbols) are also shown for comparison. Note that the dispersion curve obtained with [15] is hyperbolic and tends to that of the EMT as the dielectric thickness decreases. It is important to highlight that since both [15] and EMT do not account for spatial dispersion, the imaginary part of their respective propagation constants [Figs. 7(b) and 7(d)] are close to zero in the region of $|k_x/k_0| > 2.5$. Likewise, spatial dispersion has negligible effect on the CPR approach only when $|k_x/k_0| < 2.5$. In sharp contrast to EMT and [15], CPR exhibits a flattening of the dispersion curve (and the consequent increase in its imaginary part) beyond a threshold value of $|k_x/k_0|$ that varies with thickness, leading to the absence of propagating modes inside the HMM. For example, as seen in Fig. 7 for a thickness of 16 nm, flattening occurs for $|k_x/k_0| > 5$. Also notice that as $|k_x/k_0|$ increases the electromagnetic parameters tend to those of the metal (i.e., S_{11} tends to –1 while S_{21} tends to 0). Therefore, (21) can be rewritten as

$$\beta_z^\Delta \xrightarrow{k_x\to\infty} \frac{1}{t}\left\{\pi(2n-1) + j\log\left(\left|\frac{1}{2S_{21}^\Delta} \times\left[1-\left(S_{11}^\Delta\right)^2-\left(S_{11}^\Delta\right)^2\right]\right|\right)\right\}. \quad (26)$$

Taking only the real part of (26) we get

$$\mathrm{Re}\left\{\beta_z^\Delta\right\} \xrightarrow{k_x\to\infty} \frac{\pi(2n-1)}{t} = m\frac{\pi}{t}. \quad (27)$$

The integer m can be calculated as a function of the number of layers (N),

$$m = \mathrm{floor}\left(\frac{N}{2}\right). \quad (28)$$

Since $t = d/(1-\rho)\mathrm{floor}(N/2)$, the values where the curves flattens out can be approximated as

$$\mathrm{Re}\left\{\beta_z^\Delta\right\} \xrightarrow{k_x\to\infty} \frac{\pi(1-\rho)}{d}. \quad (29)$$

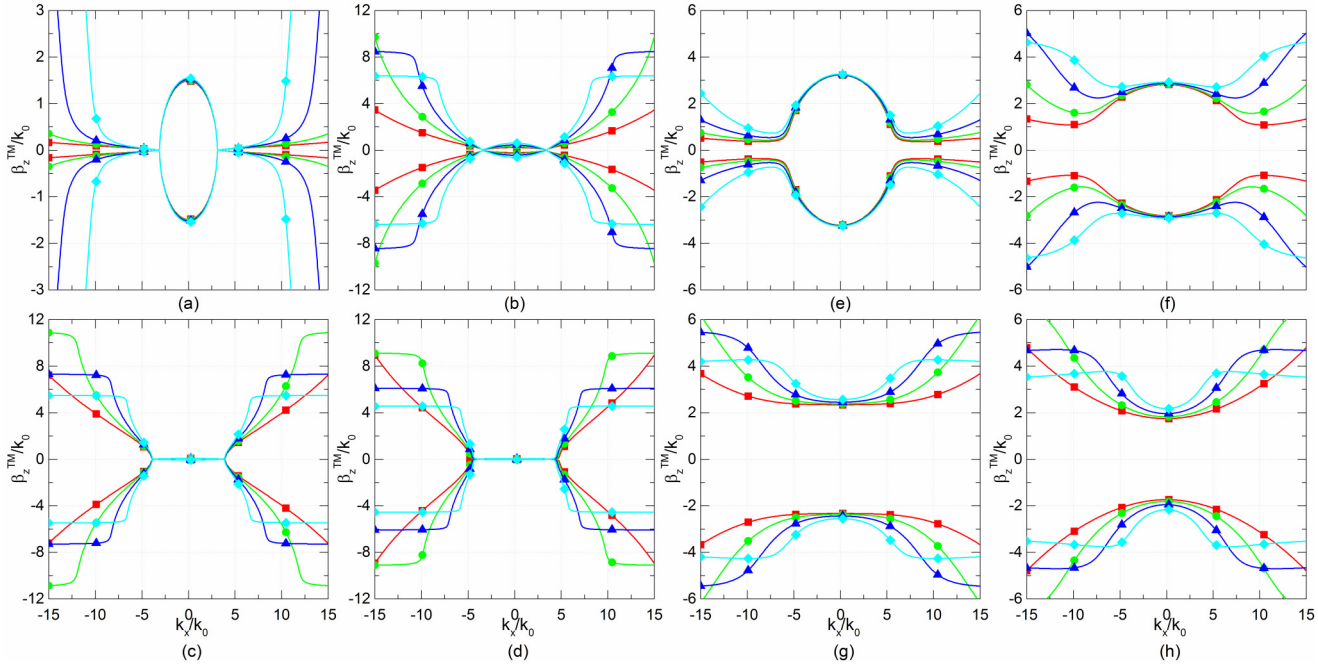

FIG. 8. Dispersion curves for Ag/TiO_2 [(a)–(d)] and Au/Si [(e)–(h)] stacks with (a,e) $\rho = 0.2$, (b,f) $\rho = 0.3$, (c,g) $\rho = 0.4$, and (d,h) $\rho = 0.5$. The dielectric thicknesses (used as a parameter) are 8 nm (squares), 16 nm (circles), 24 nm (triangles), and 32 nm (diamonds). Note that at $\rho = 0.4$ and $\rho = 0.5$, Ag/TiO_2 corresponds to a single-sheet hyperboloid while Au/Si corresponds to a two-sheet hyperboloid surface.

According to (29), the flat regions start sooner (at lower $|k_x/k_0|$ values) either for thicker layers or for higher filling factors. It is important to notice that the number of layers does not influence the point where the flattening behavior starts. The imaginary part [Fig. 7(b)] is also more significant in this region, indicating a stronger field interaction with the metal layers. The flattening out of the dispersion curve becomes more evident for a fill factor $\rho = 0.5$, as shown in Figs. 7(c) and 7(d) and according to (29). This analysis shows that the Ag/SiO_2 stack is not a good candidate for hyperbolic metamaterial for two reasons: (1) spatial dispersion can be mitigated with low fill factors but only at the expense of impractically thin metal layers; (2) high fill factors make spatial dispersion particularly problematic.

Next, we investigate two stack configurations often used for hyperbolic media [8,29]: Ag/TiO_2 and Au/Si. The polarization is TM and the wavelength is $\lambda = 600$ nm, which corresponds to $\epsilon_m = -16.075 + 0.437j$ and $\epsilon_d = 6.786$ for Ag/TiO_2, and $\epsilon_m = -9.781 + 2.045j$ and $\epsilon_d = 15.51 + 0.018j$ for Au/Si. Figures 8(a)–8(h) show the dispersion curves for both stacks with $\rho = 0.2, 0.3, 0.4$, and 0.5. The dielectric thickness is used as a parameter with values of 8, 16, 24, and 32 nm. Figures 8(a) and 8(b) show that the Ag/TiO_2 stack behaves essentially as a dielectric (not hyperbolic), and that for $|k_x/k_0| < 3$ the dielectric thickness does not play an important role in the definition of the dispersion curve. The Ag/TiO_2 stack behavior, however, does become hyperbolic for $\rho = 0.4$ and 0.5, as seen in Figs. 8(c) and 8(d), respectively, in spite of the flattening of the dispersion curve.

Regarding the Au/Si stack, the EMT approximation predicts the behavior of this structure as essentially dielectric for $\rho = 0.2$ and $\rho = 0.3$. A similar behavior is also observed with the CPR approach, as seen in Figs. 8(e) and 8(f), which predicts an elliptical dispersion profile for both these fill factors. By increasing ρ even further to 0.4 and 0.5 as shown in Figs. 8(g) and 8(h), respectively, the dispersion curves become hyperbolic. Moreover, as d (or ρ) increases so does the metal thickness. Thus, the metamaterial loss becomes significant and the dispersion curve once again flattens out.

In summary, these results show that spatial dispersion not only is always present, but also that it plays an important role in the dispersion profile for any $|k_x/k_0|$ ratio. More importantly, they show that this effect cannot be neglected, particularly in regions where the dispersion region is flat. Finally, since this flat region strongly depends on the metal thickness (i.e., it occurs for lower $|k_x/k_0|$ values when thicker metal layers are used), a careful design of the metamaterial is required to avoid this issue.

IV. CALCULATION OF THE PURCELL FACTOR

One particularly important application of hyperbolic metamaterials is in the enhancement of the Purcell factor [6–9]. This is true because hyperbolic metamaterials support high k_x values and, consequently, a much higher number of electromagnetic states [1] than ordinary materials do. As a result, the decay rate for an atom placed above these materials can be increased, thus enhancing the Purcell factor. Considering an atom at a distance q from a surface, the Purcell factor for the perpendicular orientation can be calculated as

$$P_\perp = \frac{3}{2}k_0 \int_0^\infty \frac{1}{k_z}\left(\frac{k_x}{k_0}\right)^3 (1 - S_{11}e^{2jk_z q})dk_x. \qquad (30)$$

The reflection coefficient can be calculated in four different ways: (i) using (1)–(5), which is numerically precise and accurate and treated here as a benchmark [6–9]; (ii) using

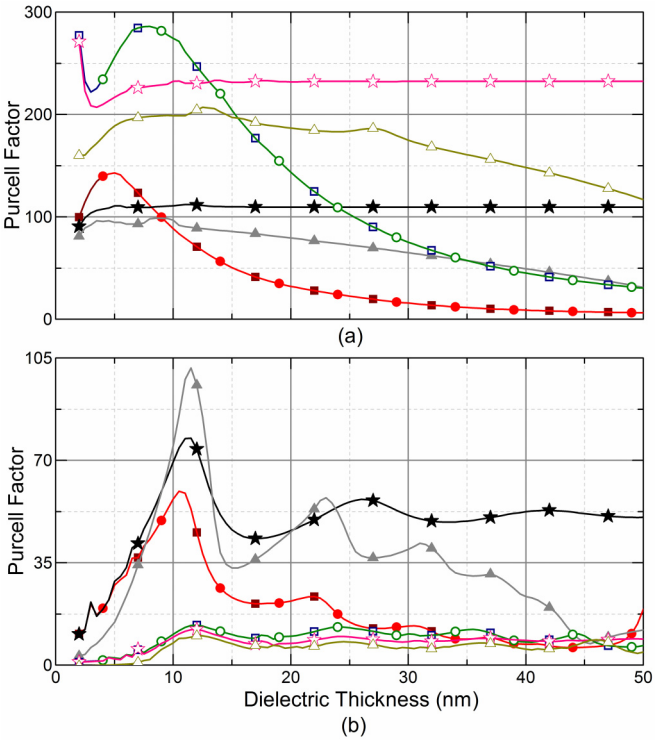

FIG. 9. Purcell factor calculated using (i) the benchmark approach (squares), (ii) the EMT approach (stars), (iii) [15] (triangles), and (iv) the CPR approach (circles). The calculation is carried out for a Rb atom 10 nm above the surface of a Ag/TiO_2 stack with $\rho = 0.3$ (hollow symbols) and 0.5 (full symbols) for $\lambda = 785$ nm (a) and 435 nm (b).

(18) and (19) with the help of the EMT approximation; (iii) using [15], and (iv) with the CPR approach. In order to show the differences among these four approaches, we consider Rb atoms 10 nm above the HMM surface, for emission wavelengths of 785 nm and 435 nm. The HMM chosen is the Ag/TiO_2 stack with two distinct filling factors, i.e., $\rho = 0.3$ and $\rho = 0.5$, and $N = 13$ layers. Figure 9(a) shows the Purcell factor calculated for 785 nm. In both cases ($\rho = 0.3$ and $\rho = 0.5$) the benchmark results (squares) and the CPR approach (circles) are in excellent agreement, indicating that the parameter extraction procedure proposed here is very accurate. The results from (ii) (stars) and (iii) (triangles), on the other hand, deviate considerably from the benchmark solution in almost the entire dielectric thickness range (except for very thin layers) as a result of spatial dispersion not being taken into account (see Figs. 7 and 8). Consequently, the Purcell factor calculated with these approaches is overestimated. The approaches (i) and (iv) are both capable of predicting this flattening behavior and correctly showing the decrease of the Purcell factor as the thickness d increases. The maximum Purcell factor for $\lambda = 785$ nm occurs for $\rho = 0.3$. As mentioned previously in this paper, the higher the value of ρ, the sooner the flat region in the dispersion curve will start and, consequently, the higher the propagation loss. This explains why the Purcell factor is larger for $\rho = 0.3$ than it is for $\rho = 0.5$. Finally, Fig. 9(b) shows the Purcell factor calculated for the emission wavelength of 435 nm. Observe that both approaches (i) and (iv) show an excellent agreement throughout the entire thickness interval. The results from (ii) and (iii), on the other hand, deviate considerably in almost the entire dielectric thickness range (except for very thin layers). Again, this is due to spatial dispersion. Differently from the previous example [Fig. 9(a)], for $\lambda = 435$ nm the Purcell factor is higher for $\rho = 0.5$ than for $\rho = 0.3$. This is a direct consequence of the stack dispersion profile not being hyperbolic for $\rho = 0.3$.

V. CONCLUSIONS

In this paper we have proposed a parameter retrieval approach in which all electromagnetic parameters of the medium are obtained and where spatial dispersion is properly taken into account. We have also relaxed the constraint on nonmagnetic metal/dielectric metamaterials. This approach was successfully applied to different metal/dielectric stacks in order to address the effects of the layer thickness, number of layers, and metal/dielectric choice on the spatial dispersion. The results have demonstrated that all investigated metal/dielectric stacks have a clear magnetic response, particularly for thicker layers. Moreover, for large $|k_x/k_0|$ the dispersion curve shows a flat region with a large imaginary part that arises due to the absence of propagating modes inside the metamaterial. This flat region is also strongly dependent on the thickness of the layers. The thicker the metal/dielectric layer is, the sooner (for lower $|k_x/k_0|$ values) the flat and lossy region appears. This behavior is a direct manifestation of the spatial dispersion and strongly affects the accuracy with which the Purcell factor is calculated. In order to illustrate this issue, we have calculated the Purcell factor for Rb atoms 10 nm above the surface of a Ag/TiO_2 stack with two distinct filling factors, i.e., $\rho = 0.3$ and $\rho = 0.5$, and $N = 13$ layers, for two emission wavelengths, i.e., 435 nm and 785 nm. The results were compared with three different approaches, namely, the benchmark result, the approach in [15], and the EMT approach. We have shown that if spatial dispersion is not properly taken into account, the Purcell factor is overestimated, as observed with both [15] and EMT approaches. However, the CPR approach has shown excellent agreement with the benchmark results.

ACKNOWLEDGMENTS

This work was supported in part by the Brazilian agencies CAPES, CNPq, and FAPESP/OSU 2015 AWARD.

[1] C. L. Cortes, W. Newman, S. Molesky, and Z. Jacob, J. Opt. (Bristol, U. K.) **14**, 063001 (2012).

[2] A. A. Orlov, S. V. Zhukovsky, I. V. Iorsh, and P. A. Belov, Photonics Nanostruct. **12**, 213 (2014).

[3] A. Poddubny, I. Iorsh, P. Belov, and Y. Kivshar, Nat. Photonics **7**, 948 (2013).

[4] Z. Jacob, L. V. Alekseyev, and E. Narimanov, Opt. Express **14**, 8247 (2006).

[5] A. Kaur, S. Banerjee, W. Zhao, J. Venkataraman, and Z. Lu, Int. J. Optics **2012**, 1 (2012).
[6] A. N. Poddubny, P. A. Belov, P. Ginzburg, A. V. Zayats, and Y. S. Kivshar, Phys. Rev. B **86**, 035148 (2012).
[7] C. Stehle, C. Zimmermann, and S. Slama, Nat. Phys. **10**, 937 (2014).
[8] D. Lu, J. J. Kan, E. E. Fullerton, and Z. Liu, Nat. Nanotechnol. **9**, 48 (2014).
[9] A. V. Chebykin, A. A. Orlov, A. S. Shalin, A. N. Poddubny, and P. A. Belov, Phys. Rev. B **91**, 205126 (2015).
[10] D. R. Smith, D. C. Vier, T. Koschny, and C. M. Soukoulis, Phys. Rev. E **71**, 036617 (2005).
[11] J. J. Barroso and U. C. Hasar, J. Infrared, Millimeter, Terahertz Waves **33**, 237 (2012).
[12] A. V. Chebykin, A. A. Orlov, C. R. Simovski, Y. S. Kivshar, and P. A. Belov, Phys. Rev. B **86**, 115420 (2012).
[13] A. Castanié, J.-F. Mercier, S. Félix, and A. Maurel, Opt. Express **22**, 29937 (2014).
[14] X. Zhang and Y. Wu, Sci. Rep. **5**, 7892 (2015).
[15] G. T. Papadakis, P. Yeh, and H. A. Atwater, Phys. Rev. B **91**, 155406 (2015).
[16] V. M. Agranovich and V. E. Kravtsov, Solid State Commun. **55**, 85 (1985).
[17] O. Kidwai, S. V. Zhukovsky, and J. E. Sipe, Phys. Rev. A **85**, 053842 (2012).
[18] A. I. Căbuz, D. Felbacq, and D. Cassagne, Phys. Rev. A **77**, 013807 (2008).
[19] A. A. Maradudin and D. L. Mills, Phys. Rev. B **7**, 2787 (1973).
[20] G. S. Agarwal, D. N. Pattanayak, and E. Wolf, Phys. Rev. B **10**, 1447 (1974).
[21] P. Halevi and R. Fuchs, J. Phys. C: Solid State Phys. **17**, 3869 (1984).
[22] P. Jewsbury, J. Phys. F: Met. Phys. **11**, 195 (1981).
[23] M. Silveirinha, IEEE Trans. Antennas Propag. **54**, 1766 (2006).
[24] J. M. McMahon, S. K. Gray, and G. C. Schatz, Nano Lett. **10**, 3473 (2010).
[25] K. R. Hiremath, L. Zschiedrich, and F. Schmidt, J. Comput. Phys. **231**, 5890 (2012).
[26] J. M. McMahon, S. K. Gray, and G. C. Schatz, Phys. Rev. B **82**, 035423 (2010).
[27] C. Menzel, C. Rockstuhl, T. Paul, F. Lederer, and T. Pertsch, Phys. Rev. B **77**, 195328 (2008).
[28] S. J. Orfanidis, *Electromagnetic Waves and Antennas*, 1st ed. (http://www.ece.rutgers.edu/~orfanidi/ewa/, 2002).
[29] H. N. S. Krishnamoorthy, Z. Jacob, E. Narimanov, I. Kretzschmar, and V. M. Menon, Science **336**, 205 (2012).